

# From observations to simulations: A neural-network approach to intracluster medium kinematics

E. Gatzuz<sup>1,\*</sup>, J. ZuHone<sup>2</sup>, J. S. Sanders<sup>1</sup>, A. Fabian<sup>3</sup>, A. Liu<sup>4</sup>, C. Pinto<sup>5</sup>, and S. Walker<sup>6</sup>

<sup>1</sup> Max-Planck-Institut für Extraterrestrische Physik, Gießenbachstraße 1, 85748 Garching, Germany

<sup>2</sup> Harvard-Smithsonian Center for Astrophysics, 60 Garden Street, Cambridge, MA 02138, USA

<sup>3</sup> Institute of Astronomy, Madingley Road, Cambridge CB3 0HA, UK

<sup>4</sup> Institute for Frontiers in Astronomy and Astrophysics, Beijing Normal University, Beijing 102206, China

<sup>5</sup> INAF – IASF Palermo, Via U. La Malfa 153, I-90146 Palermo, Italy

<sup>6</sup> Department of Physics and Astronomy, University of Alabama in Huntsville, Huntsville, AL 35899, USA

Received 24 November 2025 / Accepted 25 April 2026

## ABSTRACT

We present a systematic comparison between *XMM-Newton* velocity maps of the Virgo, Centaurus, Ophiuchus, and A3266 clusters and synthetic velocity maps generated from the Illustris TNG-300 simulated clusters. Our goal is to constrain the physical conditions and dynamical states of the intracluster medium (ICM) through a data-driven approach. We employed a Siamese convolutional neural network (CNN) designed to identify the most analogous simulated cluster to each observed system based on the morphology of their line-of-sight velocity maps. The model learns a high-dimensional similarity metric between observations and simulated clusters, allowing us to capture subtle kinematic and structural patterns beyond traditional statistical tests. We find that the best-matching simulated halos reproduce the observed large-scale velocity gradients and local kinematic substructures, suggesting that the ICM motions in these clusters arise from a combination of gas sloshing, active galactic nucleus feedback, and minor merger activity. Our results demonstrate that deep learning provides a powerful and objective framework for connecting X-ray observations to cosmological simulations, offering new insights into the dynamical evolution of galaxy clusters and the mechanisms driving turbulence and bulk flows in the hot ICM.

**Key words.** galaxies: clusters: intracluster medium – galaxies: clusters: individual: ophiuchus – galaxies: clusters: individual: centaurus – galaxies: clusters: individual: virgo – galaxies: clusters: individual: A3266 – X-rays: galaxies: clusters

## 1. Introduction

The intracluster medium (ICM) is a tenuous, X-ray-emitting plasma permeating galaxy clusters. Despite its extremely low density and high temperatures ( $\sim 10^7$ – $10^8$  K), the ICM contains several times more baryons than cluster galaxies combined (Andreon & Hurn 2010; Dai et al. 2010; Kravtsov & Borgani 2012), making it a crucial component for understanding the physics of cosmic structures. Simulations predict that the ICM should host turbulent or random motions and large-scale bulk flows arising from hierarchical merging processes (e.g., Lau et al. 2009; Vazza et al. 2011; Schmidt et al. 2017; Ha et al. 2018; Vazza et al. 2021). Additionally, sloshing motions induced by infalling substructures can generate relative bulk velocities of a few hundred kilometers per second (e.g., Ascasibar & Markevitch 2006; Ichinohe et al. 2019; Vazza et al. 2018; ZuHone et al. 2018). The central active galactic nucleus (AGN) in the brightest cluster galaxy (BCG) further contributes to ICM motions through jets and buoyantly rising relativistic plasma bubbles, potentially driving velocities of  $\sim 100$ – $500$  km s<sup>-1</sup> in surrounding gas (e.g., Brüggén et al. 2005; Heinz et al. 2010; Randall et al. 2015; Yang & Reynolds 2016; Bambic & Reynolds 2019).

Determining the kinematic properties of the ICM is therefore essential for developing a comprehensive physical picture of galaxy clusters. In this context, Sanders et al. (2020) introduced an innovative technique that leverages the instru-

mental X-ray lines in *XMM-Newton* EPIC-pn spectra to calibrate the absolute energy scale with a precision better than 100 km s<sup>-1</sup> at the Fe–K line. Using this technique, direct measurements of ICM velocities have been obtained in several systems – including the Perseus and Coma clusters (Sanders et al. 2020), Virgo (Gatzuz et al. 2022b, 2023b), Centaurus (Gatzuz et al. 2022a, 2023d), Ophiuchus (Gatzuz et al. 2023c,a), and A3266 (Gatzuz et al. 2024, 2025) – and these results have been robustly confirmed by XRISM Resolve observations (XRISM Collaboration 2025; Fujita et al. 2025; Gatzuz et al. 2026). These studies reveal a variety of velocity structures associated with both merger-driven dynamics and AGN feedback.

The launch of the X-ray Imaging and Spectroscopy Mission (XRISM) has opened a new era of direct ICM kinematic measurements. Early Resolve observations reveal a wide range of dynamical states: relaxed systems can exhibit extremely low nonthermal support (e.g., Abell 2029 shows  $\sigma_v = 169 \pm 10$  km s<sup>-1</sup> and a nonthermal pressure fraction of only  $\sim 2\%$ , XRISM Collaboration 2025). In contrast, Perseus- and Centaurus-like cool cores display measurable bulk flows consistent with sloshing, with line-of-sight velocities of  $10^2$ – $3 \times 10^2$  km s<sup>-1</sup> detected in Centaurus (XRISM Collaboration 2025; Zhang et al. 2025). XRISM measurements in Coma reveal ordered, large-scale velocity structures and modest velocity dispersions ( $\sim 200$  km s<sup>-1</sup> in multiple fields), implying coherent bulk flows at the few  $10^2$ – $10^3$  km s<sup>-1</sup> level when combining several pointings (Gatzuz et al. 2026). Overall, early XRISM results

\* Corresponding author: egatzuz@mpe.mpg.de

indicate that cool-core regions generally exhibit lower velocity dispersions than predicted by several numerical models, providing stringent constraints on turbulent pressure support and AGN feedback. Such measurements are now essential benchmarks for calibrating and testing cosmological simulations.

Comparing the observed ICM velocity structure with simulated clusters is therefore imperative, as theoretical models predict tight correlations between velocity power spectra and thermodynamic quantities such as entropy, temperature, density, and pressure (Gaspari et al. 2014; Zhuravleva et al. 2014; Mohapatra & Sharma 2019). Deep-learning methods have emerged as powerful tools for bridging observations and simulated clusters in this context. Convolutional neural networks (CNNs) have been successfully applied to tasks such as galaxy morphology classification, feature extraction in large surveys, and inference of physical properties from real and simulated data (Huertas-Company et al. 2015; Domínguez Sánchez et al. 2018; Pearson 2019). Among these architectures, Siamese CNNs – networks designed to learn a similarity metric between inputs – enable robust comparison even in limited-data scenarios. Brunel et al. (2019) employed a Siamese CNN for supernova classification using sparse light curves, and Zhang et al. (2022) applied a similar architecture to galaxy morphology classification with few labeled examples, demonstrating the general utility of deep metric learning for astrophysical inference.

Here, we present a systematic comparison between the velocity maps obtained for the Virgo, Centaurus, and Ophiuchus clusters and magnetohydrodynamic simulations, using a Siamese CNN to infer the physical conditions of the ICM. While previous deep-learning efforts have compared other ICM observables (e.g., X-ray surface brightness or temperature) across simulated clusters and observations, the velocity field remains the most complex and least constrained. We therefore focus this initial work exclusively on the kinematic structure to evaluate the performance of the Siamese framework in this challenging domain. This paper is organized as follows. Section 2 describes the *XMM-Newton* observations used in the analysis. Section 3 presents the magnetohydrodynamic simulations employed. Section 4 outlines the Siamese CNN methodology. Section 5 reports the results of the CNN-based similarity analysis. Section 6 discusses and interprets the best-matching simulated velocity maps. Finally, Sect. 8 summarizes our conclusions. Throughout this work, we adopt a  $\Lambda$  Cold Dark Matter (CDM) cosmology with  $\Omega_m = 0.3089$ ,  $\Omega_\Lambda = 0.6911$ , and  $H_0 = 67.74 \text{ km s}^{-1} \text{ Mpc}^{-1}$ .

## 2. ICM velocity maps: *XMM-Newton* observations

For this study, we used velocity maps of the Virgo (Gatuzz et al. 2022b, 2023b), Centaurus (Gatuzz et al. 2022a, 2023d), Ophiuchus (Gatuzz et al. 2023c,e), and A3266 (Gatuzz et al. 2024, 2025) clusters. Here, we summarize the procedure used to generate the velocity maps. The *XMM-Newton* EPIC data were reduced with SAS (version 19.1.0) using `epchain`, selecting single-pixel events (`PATTERN==0`), filtering soft-proton flares (threshold 1.0 cts/s), and removing bad pixels and charge-coupled device (CCD) edges (`FLAG==0`). Point sources, including central AGNs, were detected with `edetect_chain` (detection likelihood `det_ml > 10`) and masked. Following Sanders et al. (2020) and Gatuzz et al. (2022b,a), velocity maps were constructed from adaptive elliptical regions (2:1 axis ratio, tangentially oriented) sized to contain  $\sim 500$ – $750$  Fe-K counts, sampled on a 0.25 arcmin grid. Spectra from all exposures within each bin were combined and fitted in XSPEC (version 12.11.1)

using the cash statistic. The ICM emission was modeled with the `apec` model (Foster et al. 2019), except in Centaurus where a `lognorm` model accounted for its multi-temperature structure; Galactic absorption was included via `tbabs` (Wilms et al. 2000). Free parameters included redshift, temperature, metallicity, normalization (and  $\log\sigma$  for the `lognorm` model), and instrumental background lines (Cu-K $\alpha$ , Cu-K $\beta$ , Ni-K $\alpha$ , and Zn-K $\alpha$ ) were explicitly added. This procedure yields a line-of-sight velocity precision better than 100 km/s at the Fe-K line (Sanders et al. 2020).

The resulting velocity maps reveal complex and diverse kinematic structures in the ICM across the analyzed clusters. In the Virgo cluster, the velocity field shows signatures consistent with both AGN-driven outflows and gas sloshing within the core (Gatuzz et al. 2022b). For the Centaurus cluster, a clear radial velocity gradient extends to large radii, with distinct variations coincident with cold fronts (Gatuzz et al. 2022a). In Ophiuchus, a prominent redshifted–blueshifted interface is detected  $\sim 150$  kpc east of the cluster center, coinciding with X-ray surface brightness discontinuities (Gatuzz et al. 2023c). In A3266, the hot gas exhibits a globally redshifted systemic velocity relative to the cluster mean across the field of view (Gatuzz et al. 2024). Overall, most clusters lack the characteristic spiral or symmetric redshift–blueshift patterns associated with sloshing, suggesting that the line of sight is approximately perpendicular to the sloshing plane (ZuHone et al. 2016). Localized high-velocity regions may instead be linked to AGN feedback or merger-induced motions, though weak Fe-K emission in these areas increases velocity uncertainties (Gatuzz et al. 2023c).

## 3. IllustrisTNG

The IllustrisTNG project is a suite of state-of-the-art cosmological magnetohydrodynamic simulations that improve upon the original Illustris simulated clusters by incorporating more refined physical models and larger cosmological volumes (Springel et al. 2018; Pillepich et al. 2018; Naiman et al. 2018; Marinacci et al. 2018; Nelson et al. 2018, 2019). Using the moving-mesh code AREPO (Springel 2010), IllustrisTNG simulates various physical processes including radiative cooling, star formation, supernova and AGN feedback, as well as chemical enrichment. The TNG simulations have been widely applied to study cluster physics, including cool core formation (Barnes et al. 2018), black hole feedback (Weinberger et al. 2018), and ram-pressure stripping in dense environments (Yun et al. 2019). The suite comprises TNG50, TNG100, and TNG300, with box sizes of 51.7, 110.7, and 302.6 Mpc, respectively. All simulations adopt a  $\Lambda$ CDM cosmology consistent with Planck Collaboration XIII (2016) and evolve from a redshift of  $z = 127$  to  $z = 0$ . Structures are identified using the friends-of-friends (FoFs) algorithm and the SUBFIND algorithm (Springel et al. 2001; Dolag et al. 2009), and galaxies are defined as subhalos with nonzero stellar mass.

We used TNG300, which provides the largest cosmological volume and a statistically significant population of massive galaxy clusters. TNG300 contains over 280 halos with  $\log(M_{200}/M_\odot) > 14$  and several with  $\log(M_{200}/M_\odot) > 15$  (Sohn et al. 2017), with  $2 \times 2500^3$  resolution elements (dark matter particles and gas cells), a baryon mass resolution of  $m_{\text{baryon}} \sim 1.1 \times 10^7 M_\odot$ , and dark matter particle mass  $m_{\text{DM}} \sim 5.9 \times 10^7 M_\odot$ . Galaxy formation histories were traced using SubLink and LHaloTree merger trees (Rodríguez-Gomez et al. 2015; Springel et al. 2005), following the main progenitor branch at each timestep. The gravitational softening length for

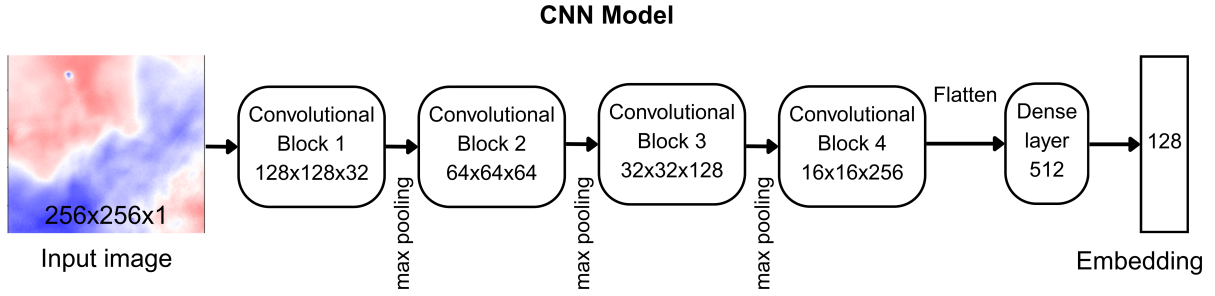


**Fig. 1.** Diagram of the CNN architecture used in our analysis. The network processes  $128 \times 128 \times 1$  input velocity maps through a series of convolution and max-pooling layers to extract hierarchical features. The resulting feature map is flattened and passed through a fully connected dense layer of 512 units, culminating in a 128D embedding vector that provides a compact, discriminative representation of the cluster kinematics.

the stellar component is  $\sim 1$  kpc at  $z = 0$ , and the minimum gas cell size can reach  $\lesssim 1$  kpc, enabling detailed modeling of ICM thermodynamics and kinematics. From this sample, we selected 40 galaxy clusters at  $z = 0$  with masses up to  $\sim 10^{15} M_{\odot}$ , consistent with the observed clusters of interest.

Synthetic observations were generated to enable direct comparison with our *XMM-Newton* maps. Following ZuHone et al. (2024), we used the pyXSIM package (ZuHone & Hallman 2016) to produce X-ray emissivity maps. Gas cells with  $T > 3 \times 10^5$  K were included, while cooler and denser star-forming phases were excluded by applying a density cut of  $\rho < 5 \times 10^{-25} \text{ g cm}^{-3}$ . X-ray emissivities (line plus continuum) in the 0.1–10 keV band were computed assuming collisional ionization equilibrium with *apec* (Foster et al. 2019), and projected maps of surface brightness and bulk velocity were constructed from the emissivity-weighted quantities. To define the reference velocity frame, the systemic velocity of the BCG was estimated from the halo stellar component. The stellar density peak was located, and the mean velocity of stellar particles within an aperture of 20–30 kpc was computed, excluding satellites and intracluster light. This velocity vector was adopted as the systemic frame, and all gas and particle velocities were re-centered accordingly before generating synthetic velocity maps in total.

To explore projection effects beyond the standard Cartesian axes ( $X, Y, Z$ ), we generated additional synthetic observations along 100 distinct lines of sight for each of the 40 halos. These orientations were defined by polar and azimuthal angles  $\theta \in [5^{\circ}, 85^{\circ}]$  and  $\phi \in [0^{\circ}, 175^{\circ}]$  in  $10^{\circ}$  intervals. The directional cosines for each line of sight were computed as

$$x = \cos \phi \cos \theta, \quad (1)$$

$$y = \cos \phi \sin \theta, \quad (2)$$

$$z = \sin \theta. \quad (3)$$

These unit vectors enabled the construction of projected maps from a broad range of viewing angles. The final comparison sample consists of 4120 synthetic velocity maps.

#### 4. Deep learning approach for velocity map matching

Traditional statistical approaches – such as  $\chi^2$  or likelihood-based tests – directly compare binned quantities or predefined features. In contrast, a machine learning framework can learn a complex, high-dimensional representation of the data, capturing subtle morphological and kinematic variations that may be overlooked by simpler statistical metrics. In this work, we adopted a deep learning approach based on velocity map data to identify

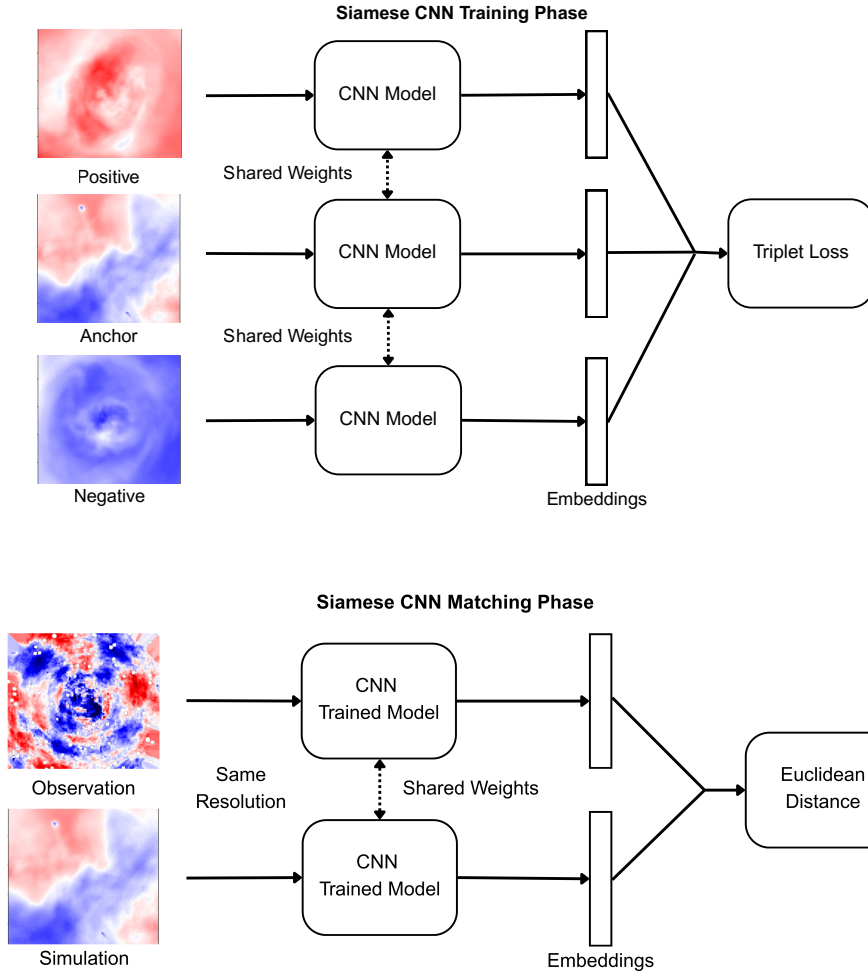
the simulated cluster that most closely resembles each *XMM-Newton* observation. Specifically, we employed a Siamese CNN consisting of two identical branches that share the same architecture and weights, allowing the model to learn a data-driven similarity metric between input maps.

Figure 1 illustrates the CNN architecture used in our analysis. The network acts as a feature extractor, transforming raw 2D pixel data into a compact numerical vector in a high-dimensional latent space. It consists of multiple convolutional layers that progressively extract hierarchical spatial and kinematic features, with max-pooling layers reducing spatial dimensionality while retaining salient features. After the final convolutional block, a flattening layer converts the feature maps into a 1D vector, which is then passed through fully connected (dense) layers to refine high-level representations. The final dense layer outputs the embedding vector—a concise numerical representation encapsulating the essential kinematic characteristics of the input velocity map. This CNN encoder serves as the backbone of the Siamese network. To ensure fair comparison, the *XMM-Newton* velocity maps were re-binned to match the spatial resolution and physical scale of the simulated clusters, using linear interpolation to preserve data integrity.

Figure 2 presents the Siamese CNN training process. The network is trained using the triplet loss function (Schroff et al. 2015), which operates on three input images: an anchor (A), a positive (P), and a negative (N). The loss function is defined as

$$\mathcal{L}_{\text{triplet}} = \max \left( \|f(A) - f(P)\|_2^2 - \|f(A) - f(N)\|_2^2 + \alpha, 0 \right), \quad (4)$$

where  $f$  denotes the CNN embedding function and  $\alpha$  is the margin parameter. This loss minimizes the distance between the anchor and positive embeddings while maximizing the distance between the anchor and negative embeddings beyond the margin. During training, network weights were updated via back-propagation, effectively organizing the embedding space such that similar velocity maps cluster together and dissimilar maps are pushed apart. Specifically, each triplet was constructed by selecting a reference velocity map (Anchor), a second projection of the same simulated cluster taken from a different line of sight (Positive), and a projection from an entirely different simulated cluster (Negative). By enforcing similarity between different viewpoints of the same physical system, the network was trained to ignore orientation-dependent morphological variations and instead extract latent kinematic features that characterize the underlying physical state of the halo. While different projections of a disturbed system may not always resemble each other visually, the triplet loss effectively forces the model to identify the deeper, invariant physical signatures common to that specific simulated cluster.



**Fig. 2.** Diagram of the Siamese CNN training phase. During training, triplets of velocity maps are passed through identical CNN encoders with shared weights. Each triplet consists of a reference (Anchor), a matched projection from the same simulated cluster (Positive), and a mismatched projection from a different simulated cluster (Negative). The network learns to produce similar embeddings for the Anchor–Positive pairs and dissimilar embeddings for the Anchor–Negative pairs by minimizing the triplet loss. This process teaches the model to recognize the underlying kinematic structure of clusters, independent of projection and resolution differences.

**Fig. 3.** Diagram of the Siamese CNN matching phase. During matching, the trained Siamese CNN compares each observed *XMM-Newton* velocity map to the full library of simulated velocity maps. Both the observed map and each simulated cluster are passed through the shared-weight CNN encoder to generate corresponding embedding vectors. Similarity between the observation and a given simulated cluster is quantified by the distance between their embeddings in the learned latent space. Simulated clusters with the smallest embedding distance are identified as the closest kinematic matches, enabling a quantitative, model-driven comparison between observed cluster dynamics and the cosmological simulations.

To mitigate overfitting and ensure unbiased performance, the simulated velocity maps were divided into independent training and validation sets. To ensure the learned representation is invariant to orientation in the focal plane, we utilized data augmentation during the training process, subjecting each input map to random  $90^\circ$  rotations and performing horizontal and vertical flips. The training set comprised 10% of the total simulated clusters. Tests confirmed that increasing this fraction yielded consistent results, demonstrating the robustness of this method. As additional validation, the network was trained on artificially generated datasets containing the *XMM-Newton* observation, perturbed versions, and purely random maps. Perturbed images were produced by applying pixel shifts and rotations, while random maps were drawn from a uniform pixel-value distribution. The network correctly identified the unperturbed observation as the closest match, confirming that it learned physically meaningful kinematic representations.

Once training was complete, the matching phase was initiated (Fig. 3). In this stage, the trained Siamese CNN branch serves as a fixed feature extractor with frozen weights. The observed *XMM-Newton* velocity map was first passed through the network to generate its unique embedding vector  $f(O)$ . Subsequently, each TNG300 simulated cluster map was processed through the same network to obtain its corresponding embedding  $f(S_j)$ . To ensure consistency, all simulated cluster maps were resampled to match the spatial resolution of the observational data. The similarity between the observation and each simulated cluster was quantified via the Euclidean distance in the learned

latent space:

$$D(O, S_j) = \|f(O) - f(S_j)\|_2 = \sqrt{\sum_{k=1}^{N_{\text{emb}}} [f(O)_k - f(S_j)_k]^2}, \quad (5)$$

where  $N_{\text{emb}}$  represents the dimensionality of the embedding vector. The embedding function  $f$  maps the complex kinematic features onto a high-dimensional manifold where the vectors are constrained to a unit hypersphere (or “normalized to the range  $[0, 1]$ ”). By operating within this normalized latent space, the reported Euclidean distances represent the relative degree of morphological and kinematic dissimilarity between clusters. A distance value approaching zero (e.g.,  $D \approx 0.002$ ) indicates a near-exact convergence of kinematic patterns within the scale of the simulated clusters sample. The simulated cluster that minimizes this distance is identified as the best match, providing a quantitative, data-driven framework for linking simulated halos to observed ICM velocity structures.

## 5. CNN-based similarity matching results

### 5.1. Hyperparameter tuning and model optimization

The performance of the Siamese CNN was optimized through a rigorous hyperparameter tuning process. Table 1 lists the parameters governing the model architecture and training dynamics, alongside their optimized values. To efficiently constrain these hyperparameters, a random search approach was employed. This

**Table 1.** Optimized hyperparameters controlling the Siamese CNN architecture.

Parameter	Function	Value
Embedding dimension	Dimensionality of the learned feature space	64
Triplet loss margin	Minimum separation between positive and negative pairs in embedding space	0.1
Learning rate	Step size during optimization	0.0001
Number of epochs	Total training iterations	100
Batch size	Number of samples per model update	32
Steps per epoch	Batch iterations per epoch	75

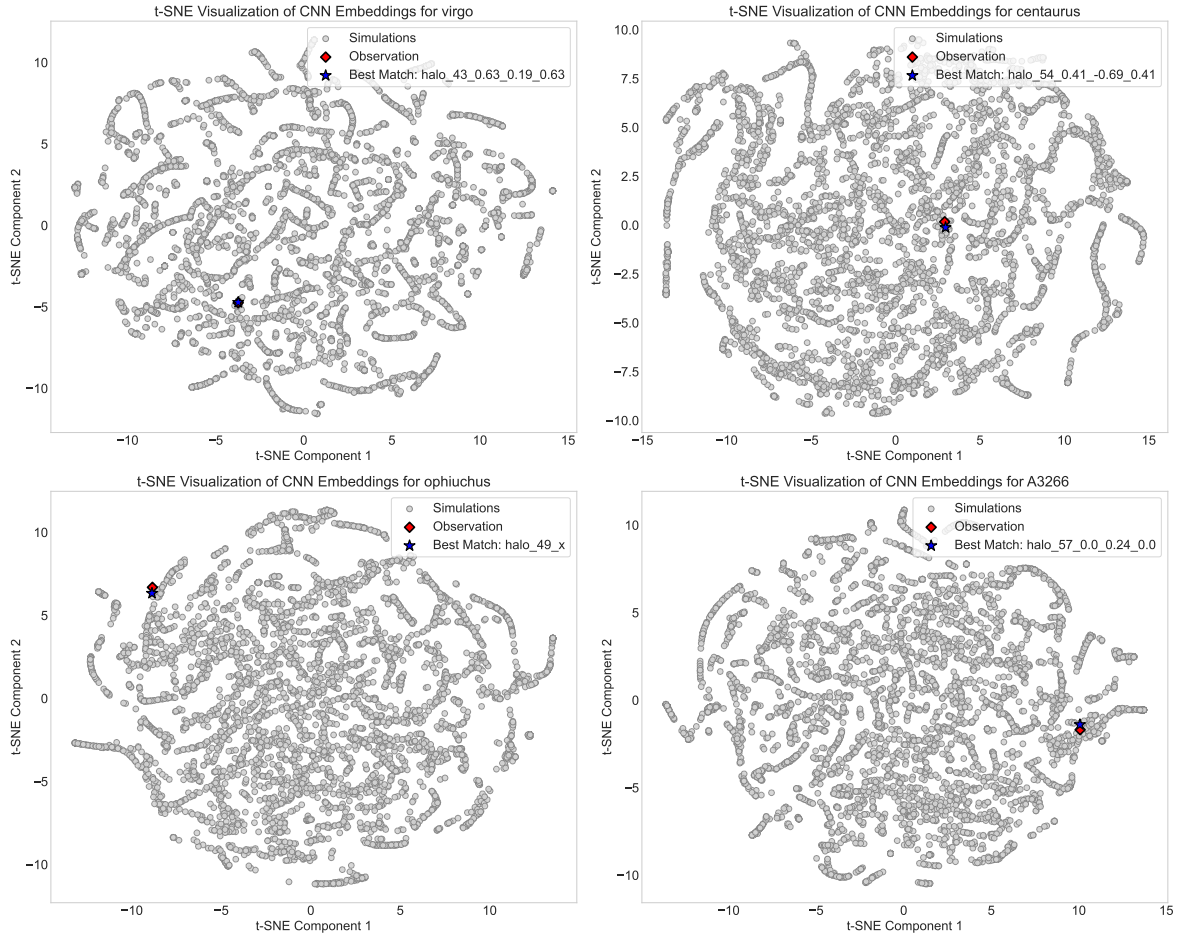


**Fig. 4.** t-SNE plots comparing the observed velocity maps of four galaxy clusters to the TNG simulation library. While all embeddings were generated using a single trained Siamese CNN, we present independent t-SNE projections for each source to clearly visualize the specific matches within the broader simulated distribution. Points represent the relative similarity of velocity maps in the latent space, with proximity indicating a closer kinematic match. The nonuniform distribution of the TNG-simulated clusters reflects underlying physical gradients and evolutionary sequences learned by the network. The axes are arbitrary, and quantitative similarity rankings (blue) are calculated based on Euclidean distances in the original high-dimensional embedding space rather than these 2D stochastic projections.

method systematically explores various parameter combinations within predefined ranges, offering a more efficient discovery of promising regions in the hyperparameter space compared to a fixed grid search. During this process, the Adam optimizer was utilized for weight updates, with the learning rate itself treated as a tunable hyperparameter to ensure optimal convergence for the velocity map features. During each trial, a new CNN branch and triplet model were initialized and trained. The primary objective was to identify the set of hyperparameters that yielded the lowest triplet loss on the training data. The weights of the best-performing model were subsequently saved and used for the final embedding generation and similarity matching. This system-

atic optimization, supported by an automated search framework, ensures a robust network configuration that effectively captures the underlying patterns in the velocity maps.

## 5.2. Embedding space visualization and analysis

To visually inspect the relationships between observed and simulated velocity maps, we employed t-distributed stochastic neighbor embedding (t-SNE) to reduce the high-dimensional CNN embeddings to a 2D space. The results are shown in Fig. 4. In this space, similar data points are represented by nearby points, while dissimilar points are farther apart. Notably, the simulated

**Table 2.** Summary of TNG300 halo properties from the best matches between *XMM-Newton* observations and simulated clusters.

Parameter	Virgo	Centaurus	Ophiuchus	A3266
Best-match halo	halo_14	halo_35	halo_2	halo_57
Projection ( $x, y, z$ )	(0.41, -0.91, 0.41)	(0.09, -0.39, 0.09)	(0.33, 0.08, 0.33)	(0, 0.24, 0)
Euclidean distance ( $d_{\text{best}}$ )	0.002	0.002	0.001	0.001
$M_{\star}(<R_{200})$ [ $M_{\odot}$ ]	$4.77 \times 10^{12}$	$4.12 \times 10^{12}$	$1.07 \times 10^{13}$	$3.20 \times 10^{12}$
$M_{\text{gas}}(<R_{200})$ [ $M_{\odot}$ ]	$6.40 \times 10^{13}$	$5.49 \times 10^{13}$	$1.44 \times 10^{14}$	$4.29 \times 10^{13}$
SFR( $<R_{200}$ ) [ $M_{\odot}/\text{yr}$ ]	4.59	1.01	1.33	5.49

clusters are not uniformly scattered; the resulting structures (e.g., filaments and curves) reflect continuous evolutionary sequences and physical gradients captured by the CNN. Each panel corresponds to a different galaxy cluster, showing the observed velocity map (red point) and its best match from the TNG300 sample based on Euclidean distance (blue point). These plots indicate that the TNG300 sample contains highly analogous objects with velocity structures closely resembling the observed ones. It is important to note that while t-SNE preserves the local neighborhood structure, the nonlinear, nonmetric nature of the projection means that 2D distances do not precisely reflect the true high-dimensional Euclidean distances used for similarity ranking.

To identify not only the single best match but also simulated clusters close in embedded features, we implemented a relative threshold. We first determined the Euclidean distance  $d_{\text{best}}$  of the single best-matching simulated cluster to the *XMM-Newton* velocity map. A simulated cluster was classified as a “very close” match if its distance  $d_{\text{sim}}$  satisfied

$$d_{\text{best}} < d_{\text{sim}} \leq d_{\text{best}} \times (1 + p), \quad (6)$$

where  $p$  is a defined percentage threshold (e.g.,  $p = 0.20$  for a 20% threshold). This approach ensures that the search for similar simulated clusters is contextual and focuses around the best-fitting halo. Applying this conservative threshold, we find that the “very close” matches for each cluster correspond to the same halo from the simulation suite, differing only by their 3D orientation. This result validates the Siamese CNN’s capability, demonstrating that the embedding space successfully captures the intrinsic structure of a halo and correctly clusters rotational variants as highly similar rather than treating them as distinct entities.

## 6. Kinematic analysis of the ICM: Observations versus simulated clusters

Table 2 lists the best-matching halos identified for each observed cluster, including their projected coordinates ( $x, y, z$ ), the Euclidean distance from the Siamese CNN comparison, and the corresponding total stellar mass, gas mass, and star formation rate (SFR) within  $R_{200}$ . Figure 5 presents the line of sights (LOS) velocity maps for these best-matching systems. In the following subsections, we compare the baryonic properties and velocity structures of the best-matching TNG300 halos with those of the corresponding *XMM-Newton* observations.

### 6.1. The Virgo galaxy cluster

The Virgo Cluster, centered on M87, exhibits complex ICM kinematics shaped by both merger activity and AGN feedback. The Siamese CNN identified halo #14 in TNG300 as

the best kinematic match to the observed LOS velocity field, with projected coordinates ( $x, y, z$ ) = (0.41, -0.91, 0.41) (Fig. 5, top left). The best-matching simulated clusters reproduces the main baryonic components of Virgo with good fidelity. At  $R_{200}$ , the simulated gas mass,  $M_{\text{gas}}^{\text{sim}} = 0.64 \times 10^{14} M_{\odot}$ , falls comfortably within the observational range of  $(0.4-1.7) \times 10^{14} M_{\odot}$  (Nulsen & Bohringer 1995; Simionescu et al. 2010; McCall et al. 2024), indicating that the TNG300 model accurately captures the global thermodynamic state and gas extent of the cluster. The stellar mass,  $M_{\star}^{\text{sim}} = 4.77 \times 10^{12} M_{\odot}$ , lies slightly below the lower limit of the observed interval  $(5.0-20) \times 10^{12} M_{\odot}$  (Ferrarese et al. 2012, 2016; Sánchez-Janssen et al. 2019; Morgan et al. 2025), suggesting a mild underestimation of star formation efficiency or past merger-driven buildup in the model. The total SFR of  $\text{SFR}^{\text{sim}} = 4.6 M_{\odot} \text{yr}^{-1}$  also resides near the lower bound of the observed range  $(5-20 M_{\odot} \text{yr}^{-1})$  (Cortese et al. 2012; Gavazzi et al. 2012; Boselli et al. 2023; Edler et al. 2024), consistent with Virgo’s quiescent nature. We note, however, that due to the limited training size and reference sets available for this study, these comparative inferences should be viewed as illustrative and interpreted with caution rather than as a definitive assessment of systemic discrepancies in the TNG300 physics.

Both the simulated cluster and the *XMM-Newton* data show a large-scale velocity gradient across the cluster core, indicative of gas sloshing triggered by a minor merger (Gatuzz et al. 2022b). In the observed map, gas within  $r < 30$  kpc is blueshifted relative to M87, while gas at larger radii is redshifted—a pattern reproduced by the best-matching TNG300 halo. At smaller scales, the *XMM-Newton* data show localized, oppositely directed velocity features ( $v_E \approx +1200$  km/s,  $v_W \approx -1500$  km/s) associated with AGN-driven gas outflows (Gatuzz et al. 2022b). While the simulated cluster captures the broad east-west velocity asymmetry, it yields smoother gradients, likely reflecting the limited spatial resolution of the AGN feedback model in TNG300, which lacks explicit jet evolution or resolved bubble dynamics (Owen et al. 2000; Forman et al. 2007). Furthermore, an inspection of the mass assembly history of the best-matched TNG halo confirms a steady growth profile without recent major merger events, consistent with the relatively relaxed kinematic state observed in the Virgo velocity maps.

### 6.2. The Centaurus galaxy cluster

The Centaurus Cluster is a cool-core system exhibiting both AGN feedback and complex gas dynamics. The Siamese CNN identified halo #35 from TNG300 as the closest kinematic analog, with coordinates ( $x, y, z$ ) = (0.09, -0.39, 0.09) (Fig. 5, top right). At  $R_{200}$ , the simulated gas mass,  $M_{\text{gas}}^{\text{sim}} = 5.49 \times 10^{13} M_{\odot}$ , lies close to the lower edge of the observed range  $(6.0-15) \times 10^{13} M_{\odot}$  (Sanders et al. 2016; Walker et al. 2013; Veronica et al.

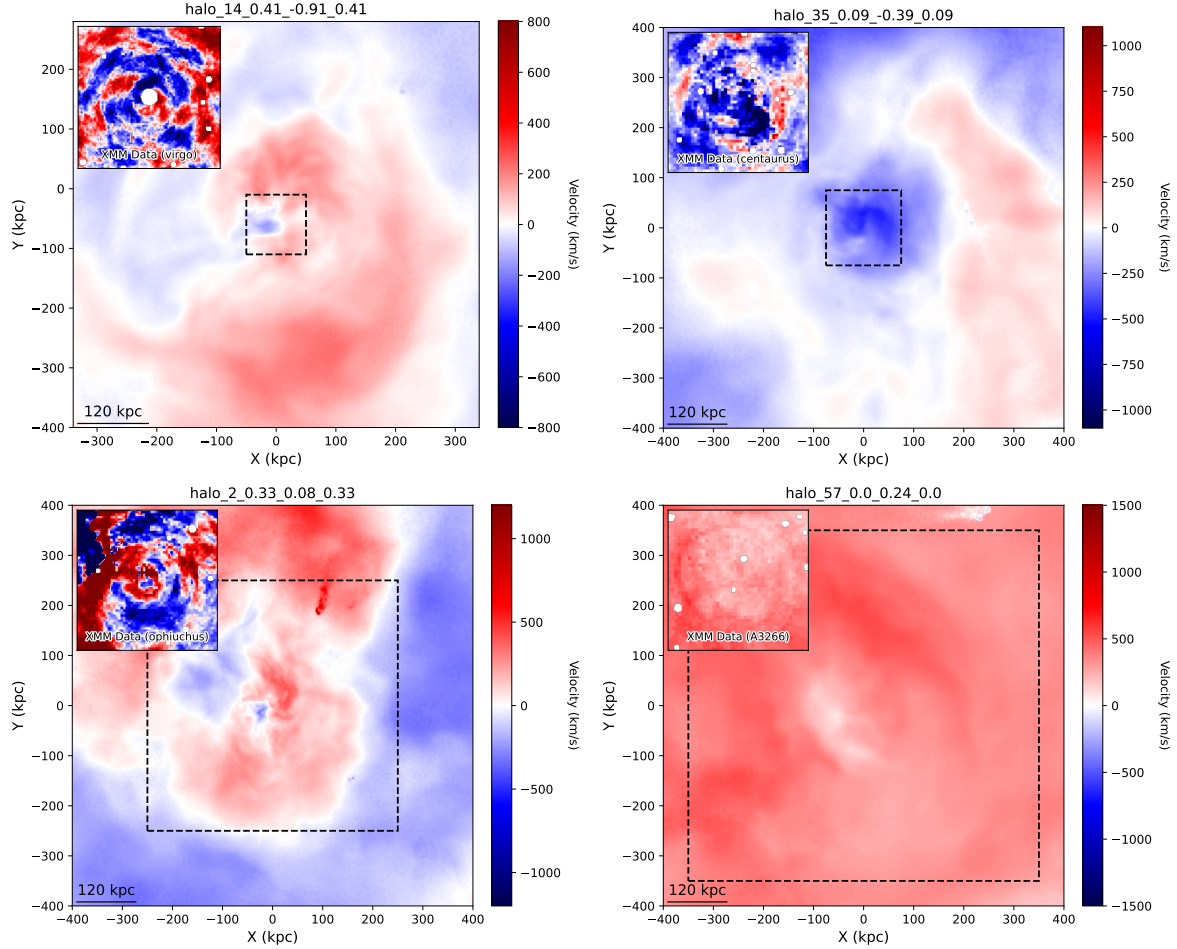


**Fig. 5.** Best-matching velocity maps from the TNG300 simulated clusters obtained with the Siamese CNN analysis for the *XMM-Newton* observations. The zoom-in panel shows the *XMM-Newton* data for a region centered on the physical origin (0, 0 kpc) of the simulated cluster. All simulated maps are presented at a fixed physical scale to maintain consistency across the sample. The apparent difference in coverage between the panels (e.g., A3266 vs. Virgo) is a result of the different angular sizes and distances of the observed clusters. Showing the full simulated extent provides crucial context for the large-scale dynamics and merger history that drive the observed core kinematics, offering insights into the broader physical environment of the matched systems. These figures illustrate kinematic similarity based on the CNN-learned metric, rather than pixel-wise visual resemblance.

2025), suggesting that the dominant baryonic component is well modeled. In contrast, the stellar mass is significantly underestimated ( $M_{\star}^{\text{sim}} = 4.12 \times 10^{12} M_{\odot}$  vs. observed  $>1.0 \times 10^{13} M_{\odot}$ ), likely reflecting either an underproduction of the BCG and intracluster light or overly strong quenching in massive halos (Misgeld et al. 2009; Saviane & Jerjen 2007; Liu et al. 2012). Similarly, the total SFR,  $\text{SFR}^{\text{sim}} = 1.0 M_{\odot} \text{yr}^{-1}$ , is lower than the observed 5–15  $M_{\odot} \text{yr}^{-1}$  range (Mittal et al. 2011; Fabian et al. 2016), consistent with the excessive suppression of residual cooling and star formation in the TNG model. We note, however, that due to the limited training size and reference sets available for this study, these comparative inferences should be viewed as illustrative and interpreted with caution rather than as a definitive assessment of systemic discrepancies in the TNG300 physics.

The *XMM-Newton* velocity map reveals a prominent blueshifted region southwest of the core, reaching  $\sim 900$  km/s (Gatuzz et al. 2022a; XRISM Collaboration 2025), with no clear spiral pattern characteristic of large-scale sloshing. The best-matching TNG300 halo reproduces this SW blueshift feature and the absence of a strong sloshing signature, implying that the observed “Centaurus wind” could result from bulk ICM motion or weak sloshing along the line of sight, rather than direct AGN

jet feedback. Small-scale redshifted patches observed near the core are less pronounced in the simulated cluster, possibly due to the limited kinematic resolution or observational noise. The absence of recent major mergers in the assembly history of the identified TNG match reinforces the interpretation of Centaurus as a system whose kinematic features are driven by internal processes rather than large-scale structural collisions.

### 6.3. The Ophiuchus galaxy cluster

The Ophiuchus Cluster is an extremely massive, X-ray luminous system exhibiting disturbed kinematics consistent with a recent or ongoing merger. The Siamese CNN selected halo #2 from TNG300 as the best match, with coordinates  $(x, y, z) = (0.33, 0.08, 0.33)$  (Fig. 5, bottom left). The simulated baryonic properties show excellent agreement with observations. The stellar mass within  $R_{200}$ ,  $M_{\star}^{\text{sim}} = 1.07 \times 10^{13} M_{\odot}$ , aligns with the measured  $(1.11^{+0.26}_{-0.43}) \times 10^{13} M_{\odot}$  (Durret et al. 2015). The gas mass,  $M_{\text{gas}}^{\text{sim}} = 1.44 \times 10^{14} M_{\odot}$ , also agrees with the observed range of  $(1-2) \times 10^{14} M_{\odot}$  well (Liu et al. 2020; Gatuzz et al. 2023c,e). The simulated SFR,  $\text{SFR}^{\text{sim}} = 1.33 M_{\odot} \text{yr}^{-1}$ , slightly exceeds the observational upper limit of  $<10 M_{\odot} \text{yr}^{-1}$  (Durret et al. 2015),

suggesting a modest overprediction of residual star formation in an otherwise quenched cool-core cluster. We note, however, that due to the limited training size and reference sets available for this study, these comparative inferences should be viewed as illustrative and interpreted with caution rather than as a definitive assessment of systemic discrepancies in the TNG300 physics.

The observed LOS velocity field shows strong radial asymmetries, with a blueshifted core and a redshifted envelope, separated by a sharp velocity discontinuity  $\Delta v \sim 2500$  km/s  $\sim 150$  kpc east of the center (Gatuzz et al. 2023c; Fujita et al. 2025). The best-matching TNG halo reproduces the overall velocity structure – including the asymmetric east-side discontinuity and large-scale velocity amplitudes ( $>1000$  km/s) – supporting the interpretation of Ophiuchus as a major off-axis merger. However, the simulated transition between the blue- and redshifted regions is smoother, consistent with the finite resolution and dissipative numerical treatment of shocks in the simulated cluster. Nonetheless, the asymmetry between the eastern and western sides of the cluster is well reproduced, indicating that the model captures the merger geometry and resulting large-scale gas dynamics. Independent validation from the TNG merger trees reveals that the best-matched halo for Ophiuchus underwent a major mass-accretion event at  $z \sim 0.32$ , providing physical support for the major off-axis merger scenario identified by our kinematic analysis.

#### 6.4. The A3266 galaxy cluster

Abell 3266 is a dynamically young system exhibiting large-scale bulk motions and substructures consistent with an ongoing major merger (Gatuzz et al. 2024). The Siamese CNN identified halo #57 from TNG300 as the best kinematic match, with projected coordinates  $(x, y, z) = (0.0, 0.24, 0.0)$  (Fig. 5, bottom right). The best-matching halo shows baryonic properties broadly consistent with observations. The stellar mass,  $M_{\star}^{\text{sim}} = 3.2 \times 10^{12} M_{\odot}$ , lies within the wide observational range  $(0.2\text{--}12) \times 10^{12} M_{\odot}$  (Gonzalez et al. 2013; Babyk et al. 2014), while the gas mass,  $M_{\text{gas}}^{\text{sim}} = 4.29 \times 10^{13} M_{\odot}$ , sits at the lower end of the measured  $(0.3\text{--}1.9) \times 10^{14} M_{\odot}$  range (De Grandi & Molendi 1999; Henriksen et al. 2000; Sanders et al. 2022). The simulated total SFR,  $\text{SFR}^{\text{sim}} = 5.5 M_{\odot} \text{ yr}^{-1}$ , remains below the observational upper limit of  $\text{SFR}_{\text{tot}} < 10 M_{\odot} \text{ yr}^{-1}$  (Quintana et al. 1996; Henriksen & Dusek 2021), suggesting a realistic, moderate level of star formation possibly sustained by merger-induced gas compression (Henriksen & Dusek 2021). We note, however, that due to the limited training size and reference sets available for this study, these comparative inferences should be viewed as illustrative and interpreted with caution rather than as a definitive assessment of systemic discrepancies in the TNG300 physics.

The observed *XMM-Newton* velocity field shows redshifted gas motions across the entire field, increasing from  $\sim 300$  km/s in the northwest to  $\sim 800$  km/s in the southeast, consistent with merger-driven bulk motion (Gatuzz et al. 2024). The TNG300 simulated cluster reproduces this large-scale redshifted gradient and the characteristic C-shaped velocity structure visible in the data, confirming that the observed ICM dynamics likely result from the projected motion of subcluster components during a major merger event (Liu et al. 2015, 2016; Ota & Yoshida 2016; Liu et al. 2018). The selection of a TNG halo with a documented major merger at redshift  $z \sim 1.4$  as the best kinematic match for A3266 confirms that our framework effectively identifies the complex velocity structures associated with significant cluster assembly events.

## 7. Caveats and limitations

The main caveats in our analysis are as follows:

- Full *XMM-Newton* response modeling was not included in generating the simulated maps due to computational cost and the complexity of multiple pointings. Instead, we directly compared the physical velocity maps, a simplification that enables efficient testing of the CNN framework. Future work will explore incorporating more realistic mock observations.
- Our machine learning approach here focuses on the line-of-sight velocity maps. Future work will aim to incorporate a broader range of robust physical observables (including X-ray surface brightness and more accurately constrained temperature and metallicity maps) into the Siamese CNN method, provided such reliable maps can be consistently extracted from the data.
- The statistical robustness of our comparative inferences is constrained by the limited training size and reference sets. With a sample of 40 TNG300 clusters used for the final comparison, the identified counterparts should be viewed as illustrative case studies for kinematic similarity. Consequently, physical interpretations of discrepancies in star formation efficiency or mass buildup between the specific simulated matches and observations should be treated as preliminary rather than a definitive assessment of systemic model performance.

## 8. Conclusions

In this work, we developed a deep-learning framework based on a CNN to quantify the morphological similarity between observed and simulated ICM velocity maps. This approach enables a fully data-driven, nonparametric comparison between *XMM-Newton* observations and TNG300 simulated clusters, providing a robust method for linking observed gas kinematics to cosmological models. The Siamese CNN was trained using a triplet-loss objective to construct a discriminative embedding space in which morphologically similar velocity structures lie in close proximity. The resulting embeddings successfully cluster different projections of the same simulated halo, demonstrating that the model learns orientation-invariant kinematic features and effectively mitigates projection effects.

A t-SNE visualization of the learned CNN embeddings further shows that each observed cluster is closely associated with a simulated halo in this feature space, indicating that the model captures physically meaningful similarities in ICM velocity morphology. The best-matching halos identified for the Virgo, Centaurus, Ophiuchus, and A3266 clusters exhibit velocity structures consistent with those observed by *XMM-Newton*, including coherent large-scale gradients and localized substructures linked to AGN feedback or merger-induced motions. In agreement with expectations from hydrodynamical simulations, these results suggest that the ICM dynamics in the analyzed systems are shaped by a combination of gas sloshing, AGN-driven outflows, and minor merger activity.

Quantitative comparisons between the observed and simulated baryonic components reveal overall consistency across the sample. The best-matching TNG300 halos reproduce the observed gas masses within uncertainties, slightly underpredict the stellar masses, and generally yield SFRs near or below observed values. In the TNG300 framework, AGN feedback becomes increasingly important within radii of approximately  $r \lesssim 50\text{--}100$  kpc, where it begins to compete with or exceed the dynamical impact of sloshing and minor mergers; outside this

region, sloshing-induced motions tend to dominate. The agreement found here supports the global validity of the TNG300 feedback model while also leaving room for refinement. If future work incorporating additional cluster properties (e.g., thermodynamic profiles, radial and azimuthal velocity statistics, and metallicity structure) confirms the systematic trends identified in this study, current assumptions regarding AGN feedback efficiency and star-formation suppression in simulated clusters may require revision.

Overall, the framework presented here provides a scalable and reproducible pathway for connecting high-resolution X-ray observations with large-volume cosmological simulations. While the current study focuses on the TNG300 suite, ongoing and future work will expand this comparison to include a broader range of high-resolution simulations, such as TNG-Cluster, Magneticum, and EAGLE, to better capture fine-scale AGN-driven features and increase statistical robustness. It establishes a foundation for future studies with next-generation X-ray observatories such as *Athena*, which will deliver unprecedented velocity precision and enable direct tests of ICM kinematics and feedback physics across cosmic time.

*Acknowledgements.* This work was supported by the Deutsche Zentrum für Luft- und Raumfahrt (DLR) under the Verbundforschung programme (Kartierung der Baryongeschwindigkeit in Galaxienhaufen). This work is based on observations obtained with XMM-Newton, an ESA science mission with instruments and contributions directly funded by ESA Member States and NASA. This research was carried out on the High Performance Computing resources of the cobra cluster at the Max Planck Computing and Data Facility (MPCDF) in Garching operated by the Max Planck Society (MPG). The full simulation outputs, including snapshot data and group catalogs, are publicly available via the ILLUSTRISTNG data release portal (<https://www.tng-project.org>).

## References

- Andreon, S., & Hurn, M. A. 2010, *MNRAS*, 404, 1922
- Ascasibar, Y., & Markevitch, M. 2006, *ApJ*, 650, 102
- Babyk, I. V., Del Popolo, A., & Vavilova, I. B. 2014, *Astron. Rep.*, 58, 587
- Bambic, C. J., & Reynolds, C. S. 2019, *ApJ*, 886, 78
- Barnes, D. J., Vogelsberger, M., Kannan, R., et al. 2018, *MNRAS*, 481, 1809
- Boselli, A., Fossati, M., Côté, P., et al. 2023, *A&A*, 675, A123
- Brüggen, M., Ruzkowski, M., & Hallman, E. 2005, *ApJ*, 630, 740
- Brunel, A., Pasquet, J., Pasquet, J., et al. 2019, arXiv e-prints [arXiv:1901.00461]
- Cortese, L., Ciesla, L., Boselli, A., et al. 2012, *A&A*, 540, A52
- Dai, X., Bregman, J. N., Kochanek, C. S., & Rasia, E. 2010, *ApJ*, 719, 119
- De Grandi, S., & Molendi, S. 1999, *ApJ*, 527, L25
- Dolag, K., Borgani, S., Murante, G., & Springel, V. 2009, *MNRAS*, 399, 497
- Domínguez Sánchez, H., Huertas-Company, M., Bernardi, M., Tuccillo, D., & Fischer, J. L. 2018, *MNRAS*, 476, 3661
- Durret, F., Wakamatsu, K., Nagayama, T., Adami, C., & Biviano, A. 2015, *A&A*, 583, A124
- Elder, H. W., Roberts, I. D., Boselli, A., et al. 2024, *A&A*, 683, A149
- Fabian, A. C., Walker, S. A., Russell, H. R., et al. 2016, *MNRAS*, 461, 922
- Ferrarese, L., Côté, P., Cuillandre, J.-C., et al. 2012, *ApJS*, 200, 4
- Ferrarese, L., Côté, P., Sánchez-Janssen, R., et al. 2016, *ApJ*, 824, 10
- Forman, W., Jones, C., Churazov, E., et al. 2007, *ApJ*, 665, 1057
- Foster, A., Smith, R., & Brickhouse, N. S. 2019, *Am. Astron. Soc. Meet. Abstr.*, 233, 251.05
- Fujita, Y., Fukushima, K., Sato, K., Fukazawa, Y., & Kondo, M. 2025, *PASJ*, 77, S270
- Gaspari, M., Churazov, E., Nagai, D., Lau, E. T., & Zhuravleva, I. 2014, *A&A*, 569, A67
- Gatuzz, E., Sanders, J. S., Canning, R., et al. 2022a, *MNRAS*, 513, 1932
- Gatuzz, E., Sanders, J. S., Dennerl, K., et al. 2022b, *MNRAS*, 511, 4511
- Gatuzz, E., Mohapatra, R., Federrath, C., et al. 2023a, *MNRAS*, 524, 2945
- Gatuzz, E., Sanders, J. S., Dennerl, K., et al. 2023b, *MNRAS*, 520, 4793
- Gatuzz, E., Sanders, J. S., Dennerl, K., et al. 2023c, *MNRAS*, 522, 2325
- Gatuzz, E., Sanders, J. S., Dennerl, K., et al. 2023d, *MNRAS*, 525, 6394
- Gatuzz, E., Sanders, J. S., Dennerl, K., et al. 2023e, *MNRAS*, 526, 396
- Gatuzz, E., Sanders, J., Liu, A., et al. 2024, *A&A*, 692, A108
- Gatuzz, E., Sanders, J., Liu, A., et al. 2025, *A&A*, 698, A94
- Gatuzz, E., Sanders, J., Liu, A., et al. 2026, *A&A*, 706, L21
- Gavazzi, G., Fumagalli, M., Galardo, V., et al. 2012, *A&A*, 545, A16
- Gonzalez, A. H., Sivanandam, S., Zabludoff, A. I., & Zaritsky, D. 2013, *ApJ*, 778, 14
- Ha, J.-H., Ryu, D., & Kang, H. 2018, *ApJ*, 857, 26
- Heinz, S., Brügggen, M., & Morsony, B. 2010, *ApJ*, 708, 462
- Henriksen, M. J., & Dusek, S. 2021, *Int. J. Astron. Astrophys.*, 11, 95
- Henriksen, M., Donnelly, R. H., & Davis, D. S. 2000, *ApJ*, 529, 692
- Huertas-Company, M., Gravet, R., Cabrera-Vives, G., et al. 2015, *ApJS*, 221, 8
- Ichinohe, Y., Simionescu, A., Werner, N., Fabian, A. C., & Takahashi, T. 2019, *MNRAS*, 483, 1744
- Kravtsov, A. V., & Borgani, S. 2012, *ARA&A*, 50, 353
- Lau, E. T., Kravtsov, A. V., & Nagai, D. 2009, *ApJ*, 705, 1129
- Liu, F. S., Mao, S., & Meng, X. M. 2012, *MNRAS*, 423, 422
- Liu, A., Yu, H., Tozzi, P., & Zhu, Z.-H. 2015, *ApJ*, 809, 27
- Liu, A., Yu, H., Tozzi, P., & Zhu, Z.-H. 2016, *ApJ*, 821, 29
- Liu, A., Yu, H., Diaferio, A., et al. 2018, *ApJ*, 863, 102
- Liu, A., Tozzi, P., Ettori, S., et al. 2020, *A&A*, 637, A58
- Marinacci, F., Vogelsberger, M., Pakmor, R., et al. 2018, *MNRAS*, 480, 5113
- McCall, H., Reiprich, T. H., Veronica, A., et al. 2024, *A&A*, 689, A113
- Misgeld, I., Hilker, M., & Mieske, S. 2009, *A&A*, 496, 683
- Mittal, R., O’Dea, C. P., Ferland, G., et al. 2011, *MNRAS*, 418, 2386
- Mohapatra, R., & Sharma, P. 2019, *MNRAS*, 484, 4881
- Morgan, C. R., Sazonova, E., Roberts, I. D., et al. 2025, *ApJ*, 987, 166
- Naiman, J. P., Pillepich, A., Springel, V., et al. 2018, *MNRAS*, 477, 1206
- Nelson, D., Pillepich, A., Springel, V., et al. 2018, *MNRAS*, 475, 624
- Nelson, D., Pillepich, A., Springel, V., et al. 2019, *MNRAS*, 490, 3234
- Nulsen, P. E. J., & Bohringer, H. 1995, *MNRAS*, 274, 1093
- Ota, N., & Yoshida, H. 2016, *PASJ*, 68, S19
- Owen, F. N., Eilek, J. A., & Kassim, N. E. 2000, *ApJ*, 543, 611
- Pearson, K. A. 2019, *AJ*, 158, 243
- Pillepich, A., Springel, V., Nelson, D., et al. 2018, *MNRAS*, 473, 4077
- Planck Collaboration XIII. 2016, *A&A*, 594, A13
- Quintana, H., Ramirez, A., & Way, M. J. 1996, *AJ*, 112, 36
- Randall, S. W., Nulsen, P. E. J., Jones, C., et al. 2015, *ApJ*, 805, 112
- Rodriguez-Gomez, V., Genel, S., Vogelsberger, M., et al. 2015, *MNRAS*, 449, 49
- Sánchez-Janssen, R., Côté, P., Ferrarese, L., et al. 2019, *ApJ*, 878, 18
- Sanders, J. S., Fabian, A. C., Taylor, G. B., et al. 2016, *MNRAS*, 457, 82
- Sanders, J. S., Dennerl, K., Russell, H. R., et al. 2020, *A&A*, 633, A42
- Sanders, J. S., Biffi, V., Brügggen, M., et al. 2022, *A&A*, 661, A36
- Saviane, I., & Jerjen, H. 2007, *AJ*, 133, 1756
- Schmidt, W., Byrohl, C., Engels, J. F., Behrens, C., & Niemeyer, J. C. 2017, *MNRAS*, 470, 142
- Schroff, F., Kalenichenko, D., & Philbin, J. 2015, 2015 IEEE Conference on Computer Vision and Pattern Recognition (CVPR), 815
- Simionescu, A., Werner, N., Forman, W. R., et al. 2010, *MNRAS*, 405, 91
- Sohn, J., Geller, M. J., Zahid, H. J., et al. 2017, *ApJS*, 229, 20
- Springel, V. 2010, *MNRAS*, 401, 791
- Springel, V., White, S. D. M., Tormen, G., & Kauffmann, G. 2001, *MNRAS*, 328, 726
- Springel, V., White, S. D. M., Jenkins, A., et al. 2005, *Nature*, 435, 629
- Springel, V., Pakmor, R., Pillepich, A., et al. 2018, *MNRAS*, 475, 676
- Vazza, F., Brunetti, G., Gheller, C., Brunino, R., & Brügggen, M. 2011, *A&A*, 529, A17
- Vazza, F., Angelinelli, M., Jones, T. W., et al. 2018, *MNRAS*, 481, L120
- Vazza, F., Wittor, D., Brunetti, G., & Brügggen, M. 2021, *A&A*, 653, A23
- Veronica, A., Reiprich, T. H., Pacaud, F., et al. 2025, *A&A*, 694, A168
- Walker, S. A., Fabian, A. C., Sanders, J. S., Simionescu, A., & Tawara, Y. 2013, *MNRAS*, 432, 554
- Weinberger, R., Springel, V., Pakmor, R., et al. 2018, *MNRAS*, 479, 4056
- Wilms, J., Allen, A., & McCray, R. 2000, *ApJ*, 542, 914
- XRISM Collaboration (Audard, M., et al.) 2025, *Nature*, 638, 365
- Yang, H. Y. K., & Reynolds, C. S. 2016, *ApJ*, 829, 90
- Yun, K., Pillepich, A., Zinger, E., et al. 2019, *MNRAS*, 483, 1042
- Zhang, Z., Zou, Z., Li, N., & Chen, Y. 2022, *RAA*, 22, 055002
- Zhang, C., Zhuravleva, I., Heinrich, A., et al. 2025, *A&A*, 707, A109
- Zhuravleva, I., Churazov, E., Schekochihin, A. A., et al. 2014, *Nature*, 515, 85
- ZuHone, J. A., & Hallman, E. J. 2016, Astrophysics Source Code Library [record ascl:1608.002]
- ZuHone, J. A., Miller, E. D., Simionescu, A., & Bautz, M. W. 2016, *ApJ*, 821, 6
- ZuHone, J. A., Miller, E. D., Bulbul, E., & Zhuravleva, I. 2018, *ApJ*, 853, 180
- ZuHone, J. A., Schellenberger, G., Ogorzalek, A., et al. 2024, *ApJ*, 967, 49

## Appendix A: Physical consistency of simulated matches

While the Siamese CNN identifies the best match based on kinematic morphology in the velocity maps, it is essential to verify that the selected halos are physically representative of the observed systems. We performed a posterior validation by comparing the global physical properties of the TNG300 parent sample against the observed ranges for each source. Figure A.1 illustrates the distribution of gas mass ( $M_{\text{gas}}$ ), stellar mass ( $M_{\star}$ ), and SFR for the 40 TNG300 halos used in this study. The shaded regions indicate the observed constraints for the Virgo, Centaurus, Ophiuchus, and A3266 clusters.

To evaluate the physical consistency of the Siamese CNN's selections, we calculated the number of simulated halos that simultaneously satisfy the observed constraints for all three physical parameters ( $M_{\text{gas}}$ ,  $M_{\star}$ , and SFR). For the Virgo cluster, out of the 40 parent halos, 15 satisfy the combined physical bounds, with the CNN-selected best match falling within this subset. Similarly, we find that five halos meet all three physical criteria for the Centaurus cluster, while six and 12 halos satisfy the combined constraints for Ophiuchus and A3266, respectively. The high degree of overlap between the kinematically selected best matches and these physically allowed regions demonstrates that the Siamese network identifies candidates that are not only morphologically similar but also physically representative of the observed systems. The high degree of overlap between the kinematically selected best matches and the physically allowed parameter space demonstrates that the Siamese CNN effectively captures the underlying physics of the ICM without explicit prior informing on global mass or star-formation scales. This confirms that the learned embeddings are physically meaningful and not merely capturing coincidental morphological similarities.

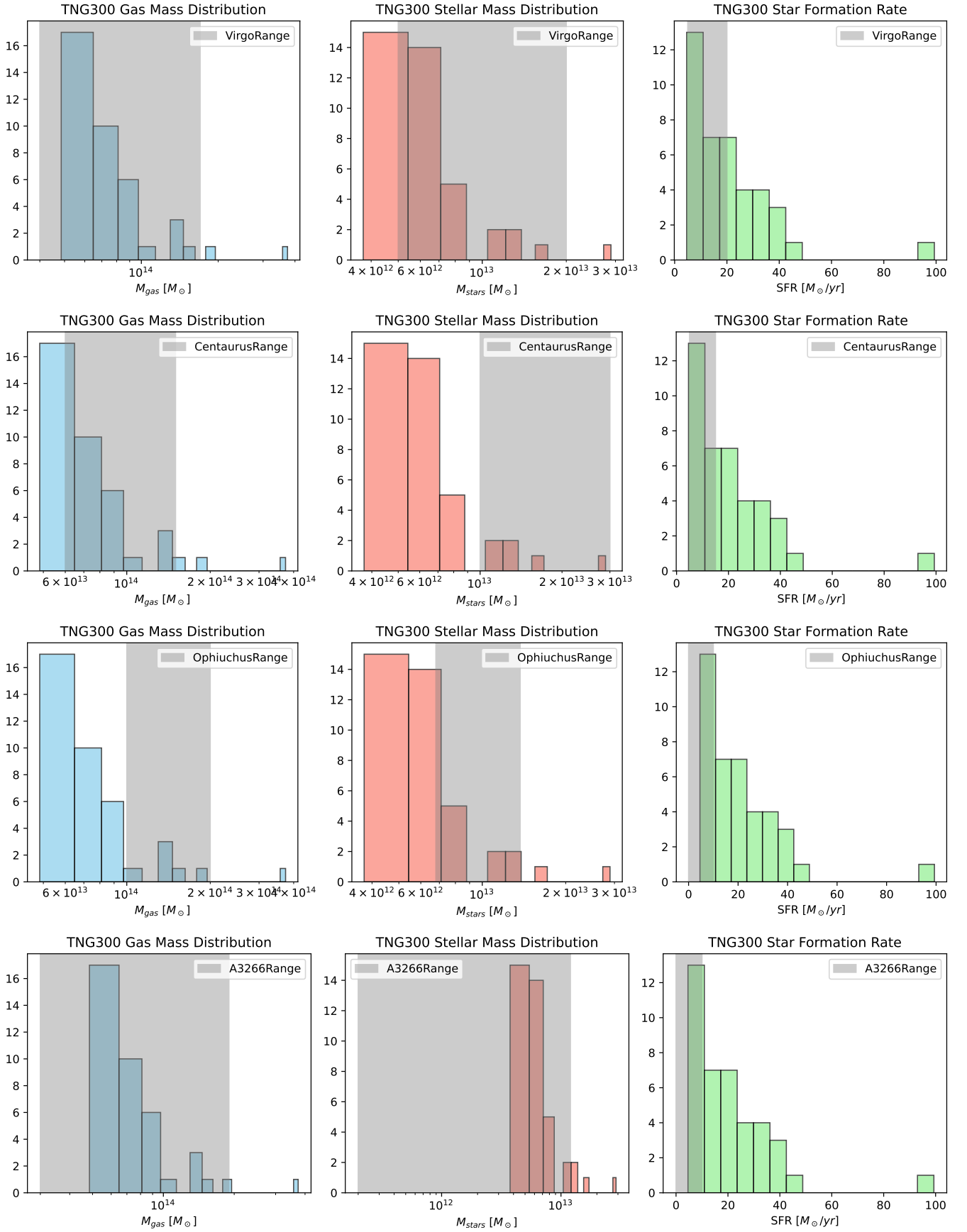


**Fig. A.1.** Distribution of physical properties across the TNG300 sample. The histograms show the frequency of gas mass (left), stellar mass (center), and SFR (right). The vertical shaded bands represent the observational uncertainties for the targeted clusters. The vertical dashed lines indicate the specific values of the best matches identified by the Siamese CNN.